Geophys. J. Int. (2003) **154,** 407–416

Experimental evidence of non-linear resonance effects between retrograde precession and the tilt-over mode within a spheroid

J. Noir, P. Cardin, D. Jault and J.-P. Masson

LGIT (CNRS and Université Joseph Fourier), B.P. 53, 38041 Grenoble Cedex 9, *France. E-mail: philippe.cardin@obs.ujf-grenoble.fr*

Accepted 2003 January 23. Received 2003 January 6; in original form 2002 May 14

SUMMARY

The Poincaré flow (also known as the tilt-over mode) in a precessing cavity filled with water is investigated experimentally. Assuming that the flow is mainly a solid-body rotation, we have used three independent techniques to determine this rotation: introduction of light ceramic particles to materialize the fluid rotation axis, pressure measurements at the cavity wall, and ultrasonic Doppler anenometry. With the latter technique, we determine the angle between the solid body rotation vector and the cavity axis indirectly, through the secondary flow – oblique shear layers which are stationary in a frame rotating at the precession rate – that the differential rotation at the boundary induces within the fluid. Rapid changes in the direction of the axis of rotation of the fluid for critical values of the rate of precession and of the rate of rotation are demonstrated. In some cases, the inclination of the fluid rotation vector with respect to the cavity axis much exceeds the inclination of the prescribed precession vector. A torque approach, which can be generalized, shows that this effect is due to a non-linear resonance between the frequencies of the Poincaré mode and of precession. As a result, we can determine the validity domain of current models of precession and nutations of planets enclosing a fluid core.

Key words: Earth's core, Earth's rotation, nutation.

1 INTRODUCTION

The dynamics of a fluid enclosed in an oblate precessing spheroidal container has been theoretically studied for over one century. The motion has been described as an uniform vorticity flow (the Poincaré flow) together with some perturbation. It has the geometry (but not the time dependence) of a nearly diurnal inertial eigenmode, which is known as the 'tilt-over mode' (Toomre 1974). The axis of the mode is contained in an equatorial plane and slowly drifts in a retrograde direction in the inertial reference frame. Stewartson & Roberts (1963) and Greenspan (1968, p.75) have pointed out a possible resonance effect between the forcing by a retrograde precession and the tilt-over mode when the non-dimensionalized precession rate, scaled by the rotation rate of the container, and the ellipticity of the interface are comparable. The rotation vector of the fluid $\boldsymbol{\omega}_\mathrm{f}$ consists of an axial component along the rotation vector of the container $\boldsymbol{\omega}_\mathrm{c}$ and of an equatorial component which becomes important when resonance is approached. Since the eigenperiod of the tilt-over mode depends on the amplitude ω_f instead of ω_c, the resonance effect is non-linear (Pais & Mouël 2001). This has been investigated by Busse (1968), who has calculated $\boldsymbol{\omega}_\mathrm{f}$ taking into account viscous effects in the boundary layer and the finite angle θ between the two rotation vectors $\boldsymbol{\omega}_\mathrm{c}$ and $\boldsymbol{\omega}_\mathrm{f}$. From his expression also, we can anticipate large changes in the direction of the vorticity vector in the case of retrograde precession. The non-linearity makes the position of the rotation axis derived from the analytical asymptotic approach of Busse (1968), in the resonance region, not intuitive. We shall show that there are values of the non-dimensionalized precession rate $\Omega = \Omega_\mathrm{p}/\omega_\mathrm{c}$, the ellipticity η, the Ekman number E and the angle α between the axis of the container and the direction of precession, for which three values of $\boldsymbol{\omega}_\mathrm{f}$ are solutions of the implicit equation obtained by Busse. In the geophysical context, excursions of $\boldsymbol{\omega}_\mathrm{f}$ may have occurred because of resonance with nutations (Toomre 1974; Greff-Lefftz & Legros 1999a,b). The precession example demonstrates that the finite value of θ may have to be taken into account in the analyses of resonance and warns against linear superposition of nutation and precession effects. Finally, we do not know to which extent the theoretical analysis of Busse is valid when $\boldsymbol{\omega}_\mathrm{f}$ strongly diverges from $\boldsymbol{\omega}_\mathrm{c}$. Numerical and experimental models are thus important to ascertain the theoretical predictions.

A recent numerical study (Lorenzani & Tilgner 2001, table 1) has accurately recovered Busse's results in the spheroidal case. In the spherical case, the resonance occurs at zero precession rate. Our numerical study (Noir *et al.* 2001a) again shows good agreement with Busse's theory, in the limit of vanishingly small viscosity, even for large inclination of the fluid rotation axis with respect to the shell rotation axis. However, the situation in which Busse (1968) predicts

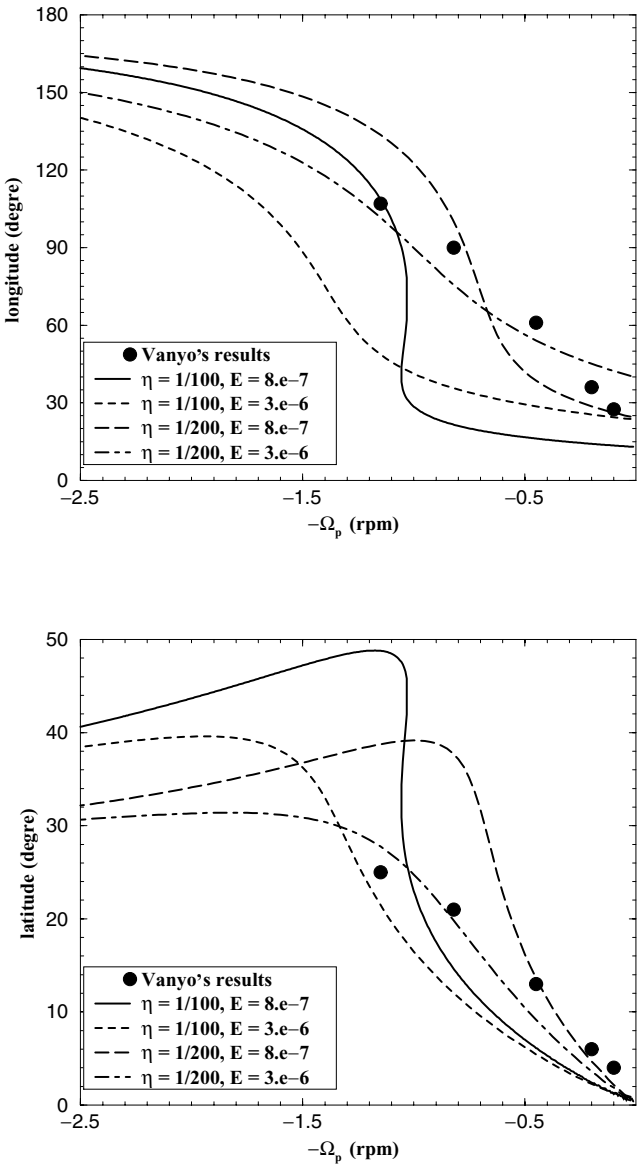

Figure 1. Comparison between the position of the axis of rotation of the fluid in Vanyo's experiment ($\eta = 1/100$, $E = 8.e-7$, Vanyo *et al.* 1995) and theoretical predictions for different ellipticities η and Ekman numbers E.

three possible values of ω_f has not been studied numerically. This happens for small values of the Ekman number, which are difficult to model.

Before our work, the single experiment series which includes determinations of the fluid rotation axis did not support the extension of the theory in the resonance domain (Vanyo *et al.* 1995). In this experiment, the angle between the rotation and precession axes is 23.5°, as in the Earth, and the Ekman number is large enough to make the solution of the Busse's equation unique except in a very narrow range of precession rates (see Fig. 1). Large excursions of the fluid rotation axis, up to 50°, are nevertheless predicted by the theory. Pais & Mouël (2001) have compared the rotation vector ω_f predicted by Busse with the experimental determinations of Vanyo *et al.* (1995). They have argued that the observations support the theory inasmuch as there is an asymmetry between the prograde and retrograde precession cases. However, we differ and reckon that the agreement remains poor: the inclination of the fluid rotation axis with respect to the spin axis of the container barely exceeds the inclination of the precession axis. Increasing the strength of the viscous friction (possibly as a result of turbulence) would explain this result, as noted by Pais & Mouël (2001), but the lack of agreement at small forcing remains puzzling. Finally, we show also on Fig. 1 that changing both the Ekman number and the ellipticity of the cavity, as advocated by Pais & Mouël (2001), does not suffice to explain individual determinations of ω_f. The best determinations of Vanyo *et al.* (1995) are derived from visualizations of geostrophic cylinders aligned with the rotation axis, which are not possible, because of turbulence, throughout most of the parameter range where large inclinations of the fluid rotation axis are predicted. Other experimental methods are thus called for. In conclusion, neither numerical calculations nor experimental works are relevant to the cases where the Busse's expression yields three different solutions for ω_f. Furthermore, inclinations of the fluid rotation axis with respect to the rotation axis of the solid boundary much larger than the inclination of the precession axis are theoretically predicted but had not been observed.

We present new experimental determinations of the fluid rotation axis near the resonance, incorporating cases corresponding to multiple solutions of the Busse's equation. The intricate part of the Busse's calculation of the fluid rotation vector is the non-linear study of the viscous boundary layer taking into account the finite angle between the rotation vector of respectively the fluid and its solid envelop. Relying instead on the linear study of Greenspan (1968) of the viscous decay of the spin-over mode in the frame of reference of constant angular velocity ω_f, we can follow a straightforward torque approach and find again the results of Busse, independently of the original derivation.

In Section 1 we present an asymptotic analysis of the determination of the mean vorticity, rephrasing the theory of Busse. Sections 2 and 3 are devoted respectively to the presentation of the experimental setup and to the techniques used to determine the components of the solid body rotation. The experimental results are given in Section 4, which introduces the final discussion in Section 5.

2 THEORETICAL DETERMINATION

We consider a spheroidal container of major semi-axis a minor semi-axis b and ellipticity $\eta = (a - b)/a$, filled with an incompressible fluid, rotating along its axis at ω_c and precessing at $\mathbf{\Omega}_p = \omega_c \mathbf{\Omega}$. Units of time and length are chosen respectively as ω_c^{-1} and a. We write the equations in the frame of reference rotating at the non-dimensionalized angular velocity $\mathbf{\Omega}$. Following Busse (1968), we look for a steady flow $\mathbf{q}$ in this frame of reference:

$$\begin{aligned} &\nabla \cdot \mathbf{q} = 0, \\ &2\mathbf{\Omega} \times \mathbf{q} + \mathbf{q} \cdot \nabla \mathbf{q} = -\nabla p + E \nabla^2 \mathbf{q}, \end{aligned} \tag{1}$$

where p is pressure and E is the Ekman number:

$$E = \frac{\nu}{\omega_c a^2}. \tag{2}$$

Busse (1968) gave also the torque balance:

$$2 \int \mathbf{r} \times (\mathbf{\Omega} \times \mathbf{q})\, dV = -\oint p \mathbf{r} \times \hat{\mathbf{n}}\, d\Sigma + E \int \mathbf{r} \times \nabla^2 \mathbf{q}\, dV \tag{3}$$

where $\mathbf{r}$ is the position vector and $\hat{\mathbf{n}}$ is the unit vector normal to Σ pointing outward.

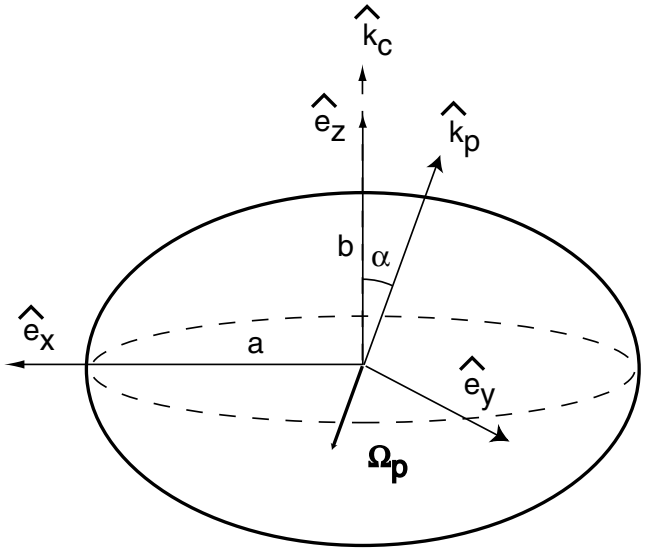

Figure 2. Frame of reference.

We will restrict our analysis to the family of steady flows, inviscid in the fluid interior, exhibited by Poincaré (1910). They have uniform vorticity and obey the no-penetration condition below the viscous boundary layer. They deviate only slightly, at the order η, from a solid body rotation. Following Busse (1968), we can check that the terms depending on η in the Poincaré expression do not appear in the torque balance at the main order in (Ω_p, $E^{1/2}$, η). In the fluid interior, we thus write:

$$\mathbf{q} = \boldsymbol{\omega}_f \times \mathbf{r} \tag{4}$$

with:

$$\boldsymbol{\omega}_f = \begin{cases} A \\ B \\ C \end{cases}. \tag{5}$$

We use here a cartesian frame ($\hat{\mathbf{e}}_x$, $\hat{\mathbf{e}}_y$, $\hat{\mathbf{e}}_z$) where $\hat{\mathbf{e}}_z$ is chosen along the minor axis of the spheroidal container, $\hat{\mathbf{e}}_x$ lies in the plane defined by ($\hat{\mathbf{e}}_z$, $\hat{\mathbf{k}}_p$) (with ($\hat{\mathbf{e}}_x.\boldsymbol{\Omega}$) > 0, see Fig. 2), and $\hat{\mathbf{e}}_z$ makes an angle α ($0 \leq \alpha \leq \pi/2$) with $\hat{\mathbf{k}}_p$. Note that ($\hat{\mathbf{k}}_p.\hat{\mathbf{e}}_z > 0$) and that retrograde precession thus means ($\Omega < 0$).

We now write the equilibrium (3) $\boldsymbol{\Gamma}_i = \boldsymbol{\Gamma}_p + \boldsymbol{\Gamma}_v$ between the inertial torque $\boldsymbol{\Gamma}_i$, the pressure torque $\boldsymbol{\Gamma}_p$ and the viscous torque $\boldsymbol{\Gamma}_v$.

2.1 The pressure torque

The balance between the centrifugal and pressure forces gives the pressure p:

$$p = \frac{(B^2+C^2)x^2 + (C^2+A^2)y^2 + (A^2+B^2)z^2}{2} - ABxy - ACzx - BCyz. \tag{6}$$

It does not change across the thin viscous boundary layer. The ellipticity enters the analysis only through the expression of $\hat{\mathbf{n}}$:

$$\hat{\mathbf{n}} = \mathbf{r} + 2\eta z \hat{\mathbf{e}}_z \tag{7}$$

Pressure stresses acting on the spheroidal boundary yield the pressure torque:

$$\boldsymbol{\Gamma}_p = I\eta \begin{pmatrix} BC \\ -AC \\ 0 \end{pmatrix}, \tag{8}$$

where I is the moment of inertia in the spherical approximation.

At this stage, we can recover the time dependence of the tilt-over eigenmode. Denoting $\chi = A + iB$, we get:

$$\frac{\partial \chi}{\partial t} = -i\eta C \chi \tag{9}$$

In an oblate spheroid, the tilt-over mode is retrograde and its eigenfrequency λ is $\lambda = -i\eta C$. We shall see that the crucial point to explain the non-linear resonance is that λ depends on C.

2.2 The precessional torque

The precessional torque $\boldsymbol{\Gamma}_i$,

$$\boldsymbol{\Gamma}_i = 2\Omega \int_V \mathbf{r} \times [\hat{\mathbf{k}}_p \times (\boldsymbol{\omega}_f \times \mathbf{r})]\, dV, \tag{10}$$

can be written as:

$$\boldsymbol{\Gamma}_i = I\Omega \begin{pmatrix} -B\cos\alpha \\ A\cos\alpha - C\sin\alpha \\ B\sin\alpha \end{pmatrix}. \tag{11}$$

2.3 The viscous torque

In this paragraph, the terms 'equatorial' and 'axial' are defined with respect to the fluid rotation axis. The eqs (8) and (11) yield $\boldsymbol{\Gamma}_p \cdot \boldsymbol{\omega}_f = \boldsymbol{\Gamma}_i \cdot \boldsymbol{\omega}_f = 0$ and, as a consequence, $\boldsymbol{\Gamma}_v \cdot \boldsymbol{\omega}_f = 0$. The axial torque is zero. As noted by Busse (1968), this implies that there is no differential rotation along $\boldsymbol{\omega}_f$:

$$\boldsymbol{\omega}_f \cdot \hat{\mathbf{k}}_c = \omega_f^2. \tag{12}$$

We will refer to this equation as the no spin-up condition.

According to eq. (12), the only relative motion between the interior and the wall is an equatorial rotation given by:

$$\boldsymbol{\delta\omega}_{eq} = \boldsymbol{\omega}_f - \boldsymbol{\omega}_c = \begin{pmatrix} A \\ B \\ C-1 \end{pmatrix}. \tag{13}$$

We rely on the linear solution of Greenspan (1968) for the viscous decay of the spin-over mode in a rotating fluid to calculate the viscous torque due to the equatorial differential rotation. The Greenspan's theory is valid in the frame of reference rotating with the fluid. We thus introduce a new Ekman number E_f and a new unit of time t_f scaled with the fluid rotation rate ω_f:

$$E_f = \frac{E}{\omega_f}, \quad t_f = t\omega_f. \tag{14}$$

According to Greenspan (1968), the time evolution of the spin-over mode, in the non-rotating frame, is given by:

$$\boldsymbol{\delta\omega}_{eq}(t) = \exp\left(\lambda^r_{so} E_f^{1/2} t_f\right)\left[\boldsymbol{\delta\omega}_{eq}(0)\cos\left(\lambda^i_{so} E_f^{1/2} t_f\right) - \frac{\boldsymbol{\omega}_f \times \boldsymbol{\delta\omega}_{eq}(0)}{\omega_f}\sin\left(\lambda^i_{so} E_f^{1/2} t_f\right)\right], \tag{15}$$

with

$$\lambda^r_{so} = -2.62 \quad \lambda^i_{so} = 0.259. \tag{16}$$

Then, reintroducing the variables E and t, the equatorial viscous torque is:

$$\mathbf{\Gamma}_v = I\frac{d(\delta\boldsymbol{\omega}_{eq})}{dt}\,|_{t=0} \tag{17}$$

$$= I(E\omega_\mathrm{f})^{1/2}\left(\lambda^r_{so}\delta\boldsymbol{\omega}_{eq}(0) - \lambda^i_{so}\frac{\boldsymbol{\omega}_\mathrm{f}\times\delta\boldsymbol{\omega}_{eq}(0)}{\omega_\mathrm{f}}\right) \tag{18}$$

$$= I(E\omega_\mathrm{f})^{1/2}\begin{pmatrix}\lambda^r_{so}A + \lambda^i_{so}\dfrac{B}{\omega_\mathrm{f}}\\ \lambda^r_{so}B - \lambda^i_{so}\dfrac{A}{\omega_\mathrm{f}}\\ \lambda^r_{so}(C-1)\end{pmatrix}. \tag{19}$$

2.4 The torque balance

The torque balance (3) projected onto $\boldsymbol{\omega}_\mathrm{f}$ (the no spin-up condition 12), $\hat{\mathbf{e}}_\mathbf{z}$, and $\hat{\mathbf{e}}_\mathbf{x}$ yields the following system of equations:

$$C = A^2 + B^2 + C^2, \tag{20}$$

$$\Omega B\sin\alpha = -(E\omega_\mathrm{f})^{1/2}\lambda^r_{so}\left(\frac{A^2+B^2}{\omega_\mathrm{f}^2}\right), \tag{21}$$

$$-\Omega B\cos\alpha = \eta BC + (E\omega_\mathrm{f})^{1/2}\left(\lambda^r_{so}A + \lambda^i_{so}\frac{B}{\omega_\mathrm{f}}\right). \tag{22}$$

Multiplying the eq. (22) by $\Omega\sin\alpha$ in order to eliminate B, we obtain:

$$\Omega A\sin\alpha = \frac{A^2+B^2}{\omega_\mathrm{f}^2}\left(\left(\frac{E}{\omega_\mathrm{f}}\right)^{1/2}\lambda^i_{so} + \eta\omega_\mathrm{f}^2 + \Omega\cos\alpha\right). \tag{23}$$

Adding the eqs (21) and (23) squared, we eliminate (A^2+B^2) and finally recover the implicit expression (3.19) of Busse (1968) for $\boldsymbol{\omega}_\mathrm{f}$:

$$\boldsymbol{\omega}_\mathrm{f} = \omega_\mathrm{f}^2\hat{\mathbf{e}}_\mathbf{z} + \frac{X\omega_\mathrm{f}^2}{X^2+Y^2}\hat{\mathbf{e}}_\mathbf{z}\times(\boldsymbol{\Omega}\times\hat{\mathbf{e}}_\mathbf{z}) + \frac{Y\omega_\mathrm{f}^2}{X^2+Y^2}\hat{\mathbf{e}}_\mathbf{z}\times\boldsymbol{\Omega}, \tag{24}$$

with,

$$X = \left(\frac{E}{\omega_\mathrm{f}}\right)^{1/2}\lambda^i_{so} + \eta\omega_\mathrm{f}^2 + \Omega\cos\alpha,\ Y = -(E\omega_\mathrm{f})^{1/2}\lambda^r_{so}, \tag{25}$$

We note that using this torque approach, we can easily include other couplings (e.g. electromagnetic friction) in the analysis.

2.5 Numerical resolution of the implicit eq. (24)

We first solve numerically the following implicit equation for the amplitude ω_f of the fluid rotation:

$$(\boldsymbol{\omega}_\mathrm{f}\cdot\boldsymbol{\omega}_\mathrm{f}) - \omega_\mathrm{f}^2 = 0, \tag{26}$$

where $\boldsymbol{\omega}_\mathrm{f}$, in the first term, is replaced by its expression (24). Then, the different components of $\boldsymbol{\omega}_\mathrm{f}$ are obtained from (24) again. We introduce the three variables $(\omega_\mathrm{f},\theta,\phi)$ to describe the axis of rotation of the fluid,

$$\cos\theta = \frac{\hat{\mathbf{e}}_\mathbf{z}\cdot\boldsymbol{\omega}_\mathrm{f}}{\omega_\mathrm{f}},\quad \theta\epsilon[0,\pi]$$

$$\cos\phi = -\frac{\hat{\mathbf{e}}_\mathbf{x}\cdot[\hat{\mathbf{e}}_\mathbf{z}\times(\hat{\mathbf{e}}_\mathbf{z}\times\boldsymbol{\omega}_\mathrm{f})]}{\sin\theta\omega_\mathrm{f}}. \tag{27}$$

Depending on the values of Ω, η and $E^{1/2}$, one or three vectors $\boldsymbol{\omega}_\mathrm{f}$ are solutions of (24). At small forcing ($|\Omega| \ll E^{1/2}, \eta$), $\omega_\mathrm{f} \simeq 1$ and the solution is unique. At large forcing the solution is unique also:

$$\boldsymbol{\omega}_\mathrm{f} = \cos\alpha\hat{\mathbf{k}}_\mathrm{p}. \tag{28}$$

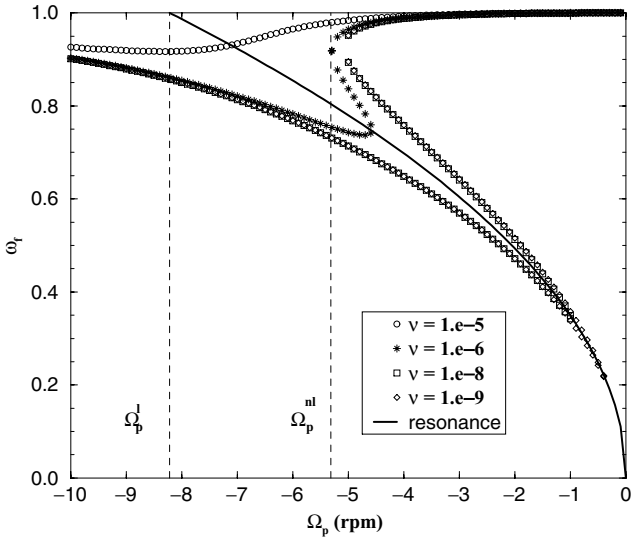

Figure 3. Amplitude of the solid-body rotation ω_f with respect to the precession rate according to the expression (24). $\alpha = 9^\circ$, $\omega_\mathrm{c} = 207$ rpm, $\eta = 1/25$ and $a = 0.125$ m. The full line shows the resonance curve $\Omega\cos\alpha = -\omega_\mathrm{f}^2\eta$. The notations Ω_p^l and Ω_p^{nl} are defined in the text.

The rotation vector is then aligned along the direction opposite to $\boldsymbol{\Omega}$ in order to minimize the precessional torque. For intermediate values of Ω, there are three solutions if the Ekman number is small enough to give full strength to the condition $\Omega\cos\alpha = -\omega_\mathrm{f}^2\eta$ of resonance between the frequencies of respectively the precessional forcing and the tilt-over eigenmode. As an example, we calculate the solutions amplitude ω_f for the parameters of one of the experiments described below changing only the value of the viscosity (Fig. 3). The linear theory ($\omega_\mathrm{f} = 1$) predicts resonance for a precession rate Ω_p^l which is very different from the rate Ω_p^{nl} (showed in Fig. 3 for $\nu = 10^{-6}$) at which the non-linear theory predicts a rapid change in ω_f and thus in the inclination of the fluid rotation axis. In the asymptotic limit of vanishing Ekman number, viscosity is important only in the vicinity of the resonance curve.

When there are three solutions, we can delineate three branches separated by the two singular points defined by $|\partial\omega_\mathrm{f}/\partial\Omega_\mathrm{p}| = \infty$. Studying how the total torque acting on the fluid $\mathbf{\Gamma} = \mathbf{\Gamma}_\mathrm{p} + \mathbf{\Gamma}_v - \mathbf{\Gamma}_i$ is modified in response to a small perturbation $\delta\boldsymbol{\omega}_\mathrm{f}$ of $\boldsymbol{\omega}_\mathrm{f}$, we investigate the stability of the different branches. A branch is unstable if there is an infinitesimal rotation $\delta\boldsymbol{\omega}_\mathrm{f}$ such that $\mathbf{\Gamma}(\boldsymbol{\omega}_\mathrm{f} + \delta\boldsymbol{\omega}_\mathrm{f})\cdot\delta\boldsymbol{\omega}_\mathrm{f} > 0$. We calculate the eigenvalues of the matrix $\partial\mathbf{\Gamma}_l/\partial(\delta\boldsymbol{\omega}_\mathrm{f})_m$ where l and m denote cartesian axes. On the first and third branches, respectively from $\Omega_\mathrm{p} = 0$ to Ω_p^{nl} and from the second singular point to $\Omega_\mathrm{p} = -\infty$, the three eigenvalues stay negative, proving stability. In contrast, one eigenvalue is positive on the second branch, showing that these solutions are unstable and cannot be realized. Such a pattern is common in non-linear dynamics (Manneville 1990).

We discuss now how this theory accounts for the experimental observations.

3 EXPERIMENTAL SETUP

The apparatus consists of a spinning spheroidal cavity filled with water, set up on a slowly rotating horizontal turntable (Fig. 4). The spheroidal cavity has been machined inside two cylindrical plexiglass blocks with a 0.02 mm precision. The outer radius of the cylindrical casing is $R_\mathrm{c} = 150$ mm, the major semi-axis of the

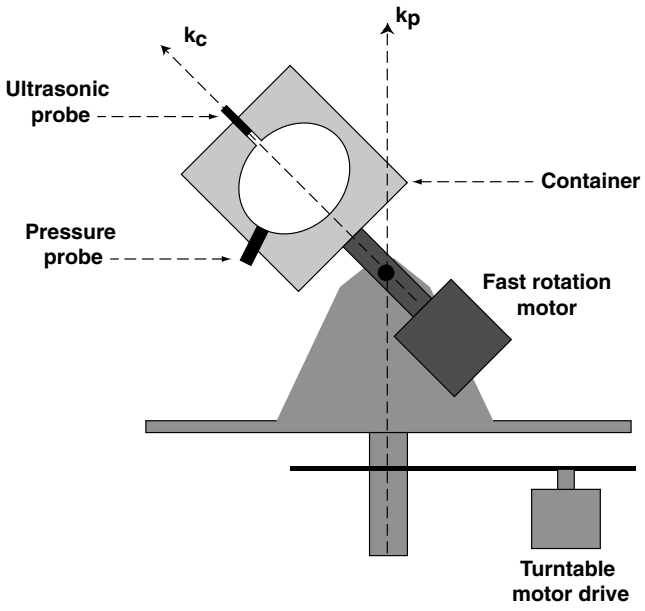

Figure 4. Experimental setup.

Table 1. Technical characteristics of the experimental setup.

α	0 to 45°
Ω_p	± 0.1 to ± 10 rpm
ω_c	50 to 1600 (300) rpm
E	$3.8 \times 10^{-7} (2. \times 10^{-6}) - 1.2 \times 10^{-5}$

cavity is $a = 125$ mm, and the ellipticity η is 1/25. A 3-kW brushless motor is used to impose the fast rotation $\boldsymbol{\omega}_c$ of the container with a stability of the angular velocity within 0.1 per cent. The rotation $\boldsymbol{\Omega}_p$ of the turntable is achieved using a second brushless motor with the same stability, and two pulleys and a transmission belt to ensure the reduction speed factor. The angle α between the axis of the rotation table and the axis of the cylinder is adjustable. We estimate its accuracy as 0.2°. The ranges for the different parameters in this experiment are summarized in Table 1. Most of the results presented below have been obtained using a malleable shaft to limit the pollution of the recorded signals by electromagnetic noise from the motors. With this device, the rotation rate ω_c cannot exceed 300 rpm. For high spinning rates of the container an air bubble, due to a dynamic deformation of the cavity, appears at the top. By measuring the amount of water needed to fill up the spheroid, we have estimated the volume change. Assuming an homogeneous deformation of the container, the radius a_d under fast rotation is calculated. For $\omega_c = 700$ rpm, $(a_d - a)$ is of the order of 0.1 mm and can be neglected.

4 EXPERIMENTAL TECHNIQUES TO DETERMINE THE AXIS OF ROTATION OF THE FLUID

4.1 Determination of the axis by direct visualization

We have performed direct visualizations of the axis using light ceramic balls in suspension in water. The particles are almost spherical, of radius $r = 40$–70 μm, and of density $\rho = 700$–800 kg m^{-3}. The balls are subject to both centrifugal acceleration and gravity, the former inducing a motion of the particles toward the axis of rotation and the latter a slow motion along the axis of rotation. During the time of an experiment (1–2 h), at low precessional forcing, we observe that the particles are collected on a well defined line. To visualize the ceramic balls we use a plane sheet of light that can be rotated around the symmetry axis of the cavity. At the beginning of the experiment, the light plane contains $\hat{\mathbf{e}}_z$ and $\boldsymbol{\Omega}_p$ and corresponds to $\phi = 0$ (see eq. 27). After a transient regime, the light sheet is rotated until most of the straight line of ceramic balls is contained inside. This gives us the longitude ϕ of the axis of rotation of the fluid. The colatitude is measured on a picture taken at a right angle to the light plane.

4.2 Determination of the axis by pressure measurements

This second method is based on the measurement of the pressure exerted by the fluid on the wall of the container. A pressure sensor, 1.262 cm in diameter, is screwed inside the wall of the cavity at a distance $h = 3$ cm below the equatorial plane. The pressure probe is a piezo-electric transducer with a dynamic range of [0.0007–34.5] kPa. Only the non-stationary components of the pressure of frequency in excess of 0.5 Hz are measured. The pressure signal is then amplified in the frame rotating with the cylinder at $\boldsymbol{\omega}_c$ and is transferred to the laboratory frame through a malleable shaft and a single electromagnetically shielded slip-ring. Finally, the sampling frequency has been chosen within the range 1.0–2.5 kHz, and each record (50 000 measurements) has a time duration of 20–50 s.

We assume again that the flow is dominantly a solid-body rotation along an axis $\boldsymbol{\omega}_f$ of colatitude θ and longitude ϕ as defined above. We express the pressure as:

$$p = p_c + p_h = \rho \frac{\omega_f^2}{2} s^2(t) - \rho(\mathbf{g}.\mathbf{r}), \tag{29}$$

where $s(t)$ is the distance between the axis of the fluid and the sensor,

$$s^2(t) = \left| \frac{\mathbf{r} \times \boldsymbol{\omega}_f}{\omega_f} \right|^2, \tag{30}$$

and

$$\mathbf{r} = \begin{pmatrix} R(h) \\ 0 \\ -h \end{pmatrix} \qquad R(h) = \sqrt{a^2 - \frac{h^2}{(1-\eta)^2}}. \tag{31}$$

The index 'c' is introduced to contrast centrifugal terms with hydrostatic terms denoted with the index 'h'. Since the axis of the fluid rotates in a retrograde direction in the frame linked to the shell, the distance s is time dependent. For $h \neq 0$, the theoretical pressure signal contains Fourier components of frequency, 0, ω_c and $2\omega_c$:

$$\begin{aligned} s^2(t) = {} & R^2(h) + \sin^2(\theta) \left[h^2 - \frac{R^2(h)}{2} \right] \\ & + 2hR(h) \cos(\theta) \sin(\theta) \cos(\omega_c t - \phi) \\ & - \sin^2(\theta) \frac{R^2(h)}{2} \cos[2(\omega_c t - \phi)]. \end{aligned} \tag{32}$$

We write the centrifugal pressure of frequency respectively ω_c and $2\omega_c$ as:

$$\begin{aligned} p_c^1 &= A_c^1 \cos(\omega_c t - \phi) \\ p_c^2 &= A_c^2 \cos[2(\omega_c t - \phi)] \end{aligned} \tag{33}$$

with

$$\begin{aligned} A_c^1 &= \rho \omega_f^2 h R(h) \cos(\theta) \sin(\theta) \\ A_c^2 &= -\rho \frac{\omega_f^2}{4} R^2(h) \sin^2(\theta). \end{aligned} \tag{34}$$

The exponents '1' and '2' denote components of frequency respectively ω_c and $2\omega_c$. We have chosen the origin of phase such that for $\omega_c t = 2k\pi$ the probe is located in the half plane $(\hat{\mathbf{e}}_z, \mathbf{\Omega}_p)$. The hydrostatic pressure p_h^1 is monochromatic of frequency ω_c:

$$p_h^1 = A_h^1 \cos(\omega_c t) \tag{35}$$

with

$$A_h^1 = \rho g R(h) \sin\alpha \tag{36}$$

The hydrostatic signal does not depend on the rate of precession. With $\Omega_p = 0$, the fluid rotates along the axis of the shell, $\theta = 0$, and the measured pressure signal should reduce to p_h^1. An optical sensor, accurately calibrated by the maxima of the hydrostatic pressure at zero precession rate, gives the phase of the signal.

Keeping α and ω_c constant throughout a series of experiments, the determination of the direction of the axis of rotation is performed in two steps. We first record simultaneously the pressure signal and the positioning pulses for $\Omega_p = 0$. We infer A_h^1 from the Fourier spectrum of the pressure. Then the system is put into precession and after a few spin-up times, we record simultaneously the pressure signal p and the positioning pulses. The pressure signal is then the sum of the centrifugal and hydrostatic contributions:

$$p = \underbrace{p_h^1 + p_c^1}_{p^1} + p_c^2, \tag{37}$$

where:

$$p^1 = A^1 \cos\left(\omega_c t - \phi^1\right), \tag{38}$$

with

$$\begin{cases} A^1 \cos(\phi^1) - A_h^1 = A_c^1 \cos(\phi), \\ A^1 \sin(\phi^1) = A_c^1 \sin(\phi). \end{cases} \tag{39}$$

The two components p^1 and p_c^2 are extracted by data processing involving a numerical Butterworth filtering. From the Fourier spectrum of p^1 and p^2, we obtain A^1 and A_c^2 and from the set of eqs (39), we calculate A_c^1 and ϕ. We can then determine the colatitude of the fluid rotation axis:

$$\theta = \arctan\left(\frac{4h}{R(h)}\frac{A_c^2}{A_c^1}\right). \tag{40}$$

Finally, the pressure signal can be calibrated from the eq. (36) and then the equations (34) yield also the amplitude ω_f. We can then redo this sequence of data analysis for another value of the precession rate.

4.3 Indirect determination of the latitude of the axis by Ultrasonic Doppler anenometry

Within slowly precessing spheroids, oscillating conical shear layers result from boundary layer breakdown at the critical latitude at $\pm 30^\circ$ with respect to the axis of rotation of the fluid. We have shown that the velocity along the oblique internal shears scales as $|\boldsymbol{\omega}_c \times \boldsymbol{\omega}_f| E_f^{1/5}/\omega_f$ (Noir *et al.* 2001a), where E_f again is the Ekman number based on the fluid rotation. Relying on ultrasonic Doppler anenometry measurements of the radial component of the velocity, we have previously reported experimental evidence of these inertial waves of diurnal frequency (Noir *et al.* 2001b). Shear layers are localized on two cones symmetrical about the fluid rotation axis. Their observation thus gives us an indirect access to the inclination of $\boldsymbol{\omega}_f$ with respect to the cavity symmetry axis. An ultrasonic pulse of frequency 4Mhz is emitted toward the fluid interior by a probe located in a hole at the top of the cavity. Pollen particles in the fluid reflect back a part of the wave in the direction of the probe with a shift in frequency that depends on the component of the velocity along the shooting line. The probe is fixed at the North pole of the cavity (see Fig. 4) and the shooting line is aligned with the axis of the cavity. Because the velocities are measured along $\boldsymbol{\omega}_c$, they are not affected by the rotation of the probe together with the Plexiglas box. Thus, we measure motions in the frame of reference of the precession turntable. We confront the experimental profiles of radial velocity with synthetic profiles obtained from numerical simulations of the flow induced within a rapidly rotating spherical cavity by an equatorial differential rotation of the boundary. The beam is collimated on a distance of 5 cm before diverging with an angle of 5°. Thus, the best lateral resolution is obtained near the probe. We have partly taken this effect into account by assuming, in the calculation of the synthetic signal, that a conical volume of semi-angle 4° and of apex, the probe surface, is sampled by the beam. By trial and error, we determine the angle θ between the beam axis and the fluid rotation axis that ensures the best agreement between measured and synthetic profiles. Note that the amplitude of the radial velocity depends also on θ since the amplitude of the differential rotation between the fluid and its boundary is $\omega_c \sin\theta$.

Finally, before presenting our own experimental results, let us recall that we have used (Noir *et al.* 2001a) a fourth method to obtain the amplitude of the fluid solid body rotation and interpret an experiment of Malkus (1968). This author measured the motion relative to the container of a dye introduced in the flow along a radius. We used the average angular drift of the dye line to infer the component of the solid body rotation along $\hat{\mathbf{k}}_c$ and we identified it to $(\boldsymbol{\omega}_f^2 - 1)\omega_c$ (see 24).

5 EXPERIMENTAL RESULTS

In Fig. 5(a) we show an example of the straight structure of ceramic balls located along the axis of the fluid as it appears for $\alpha = 25^\circ$ and $\omega_c = 300$ rpm for low retrograde precession. For a given set of parameters (ω_c, α), beyond a critical value of Ω_p, the ceramic balls are not located along a straight structure but are instead scattered in the volume (Fig. 5b). In such a case, it is impossible to determine the direction of the axis.

In Fig. 6, we show the longitude and colatitude determined by both direct visualization and pressure measurements for $\omega_c = 300$ rpm, $\alpha = 25^\circ$ and -5.5 rpm $< \Omega_p < 0$. The pressure measurements have been achieved with a preliminary version of the experimental set-up without the malleable shaft and with two non-shielded electrical slip-rings. We expect that these first measurements are less accurate than the later measurements discussed below and we do not give error bars. For the ceramic balls technique, when rotating the plane sheet of light, the error bars correspond to a range of 10° around an average longitude within which we observe the same pattern of ceramic balls. When measuring the colatitude on the photography, the thickness of the structure leads to an error within 5°. The good agreement between the two sets of estimates shows that the two methods are consistent for small inclinations of the fluid rotation axis with respect to the cavity symmetry axis. For larger inclinations, the ceramic balls are too much scattered to give useful results.

In Fig. 7, we present the determination of ϕ and θ for $\alpha = 9^\circ$ and $\omega_c = 207$ rpm using pressure measurements. We also plot the analytically predicted values and the estimates of θ obtained from ultrasonic Doppler anenometry. The dispersion of the determinations of ϕ and θ obtained through repeated pressure measurements

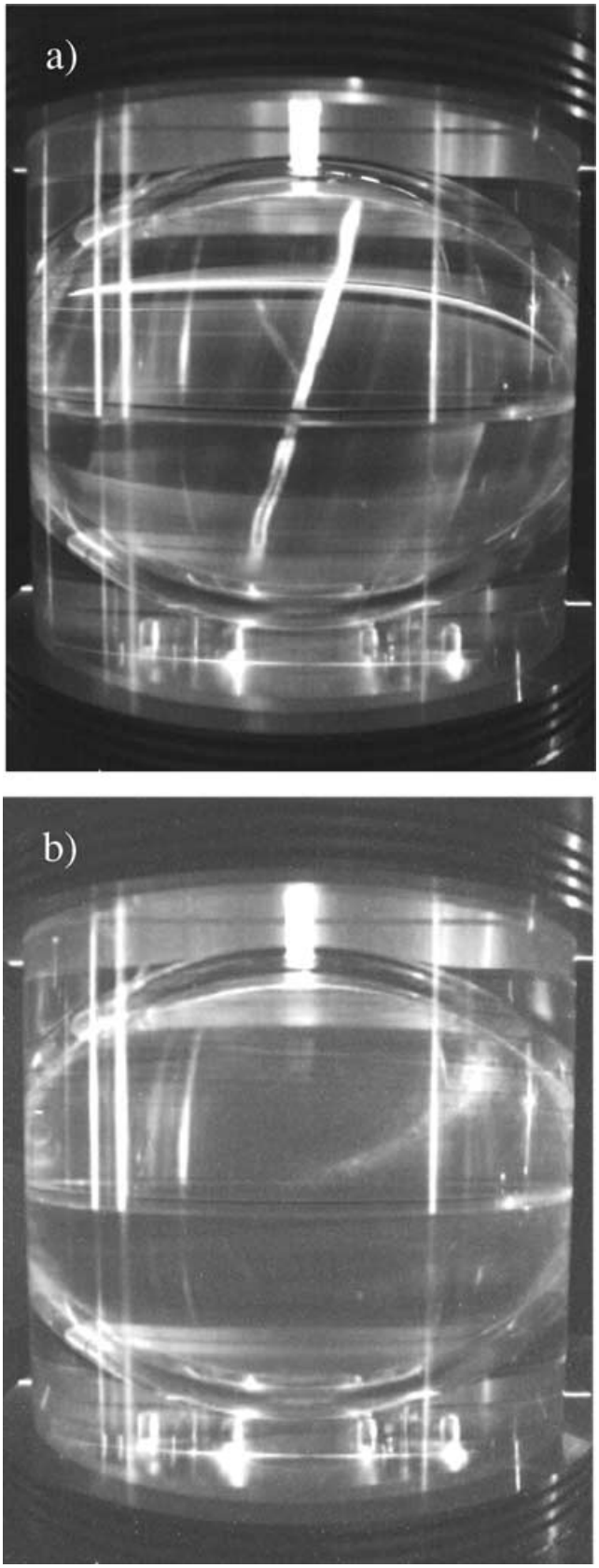

Figure 5. Direct visualization of the axis of rotation of the fluid using ceramic balls. $\omega_c = 300$ rpm, $\alpha = 25^\circ$ a) $\Omega = -4$ rpm, b) $\Omega = -6.6$ rpm.

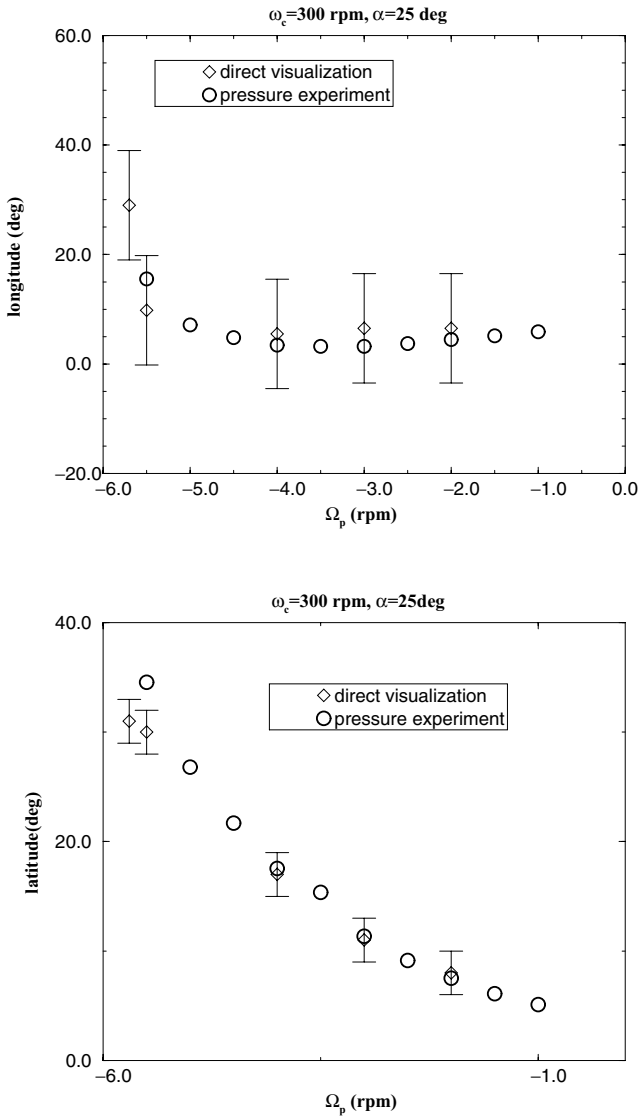

Figure 6. Longitude ϕ and colatitude θ of the axis of rotation of the fluid obtained from direct visualizations (diamonds) and pressure measurements (circles). $\omega_c = 300$ rpm, $\alpha = 25^\circ$.

at $\Omega_p = -2, -4, -5, -6, -8$ rpm gives an estimate of the precision of the method. We reckon that there are large errors at small precession rate because of a noise with frequency $2\omega_c$ in the pressure signal, already apparent at ($\Omega_p = 0$), that swamps the centrifugal pressure signal when the latter is small. We do not know how this noise is affected by precession but we show also estimates of ϕ and θ (square symbols) obtained after the modelling of a noise with frequency $2\omega_c$ that we assume independent of the precession rate to evaluate its influence on the determination of θ, ϕ and ω_f. At small precession rates, the ultrasonic Doppler signal can be well modelled (Fig. 8). At larger rates, it does not compare well with synthetic signals. Thus, we have much more confidence in the results indicated by open circles than in those indicated by full circles (Fig. 7). When the two techniques can be compared (determination of the inclination of the fluid rotation axis), they agree remarkably well. We demonstrate a sudden jump of the inclination θ of the fluid rotation axis to values that are much larger than the inclination of the precession

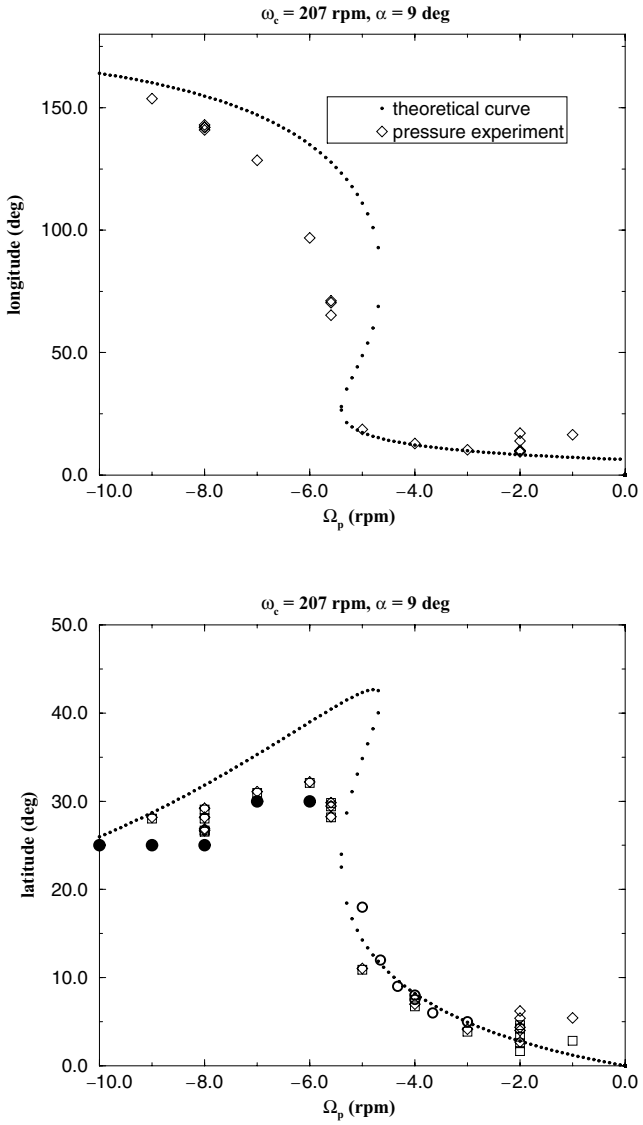

Figure 7. Longitude ϕ and colatitude θ of the axis of rotation of the fluid. The dotted lines show the solution of the asymptotic analysis introduced in Section 2. Diamond and square symbols refer to pressure measurements respectively with and without the modelling of a noise of frequency 2 ω_c independent of the precession rate. Circles show estimates from ultrasonic Doppler anenometry (see the text for the meaning of the two families of circles). Pressure and Ultrasonic Doppler measurements $\alpha = 9^\circ$, $\omega_c = 207$ rpm.

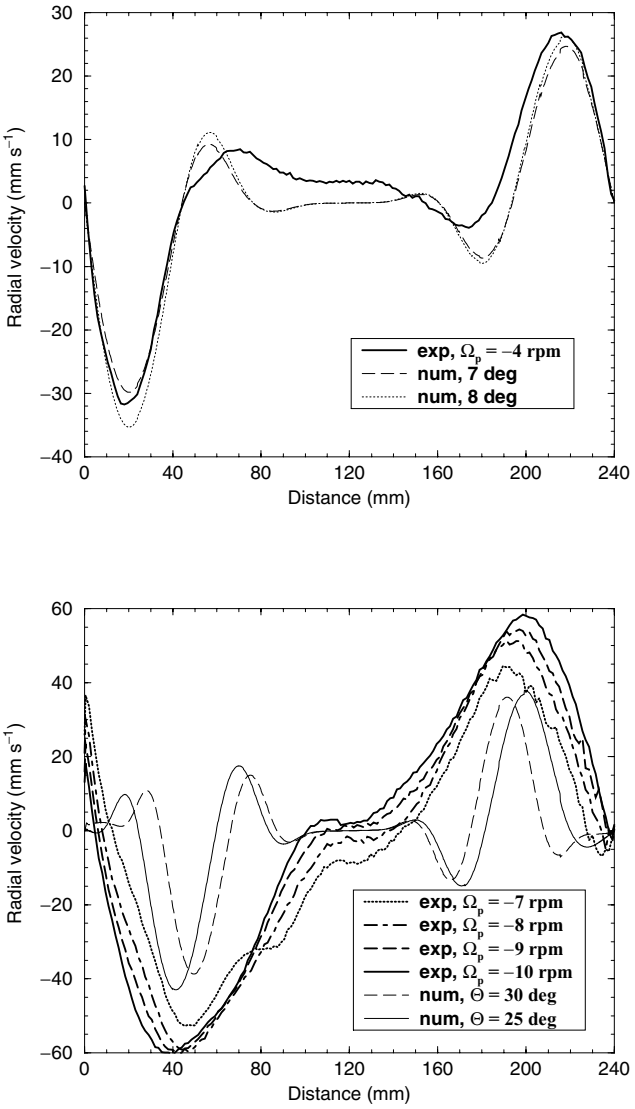

Figure 8. Comparison between measured and synthetic profiles of radial velocity using ultrasonic Doppler anenometry. $\omega_c = 207$ rpm, $\alpha = 9^\circ$ top: $\Omega = -4$ rpm, bottom: $\Omega \leq -7$ rpm.

axis and this happens for the precession rate Ω_p^{nl} that is theoretically predicted. According to the ultrasonic Doppler anenometry, the circulation within the cavity does not reduce to a solid body rotation and its accompanying secondary motion for precession rates larger than Ω_p^{nl}. On the other hand, according to the pressure measurements, the expression (24) still predicts reasonably well $\boldsymbol{\omega}_f$. This is still more evident at smaller rotation rates ω_c (see Fig. 9 for $\omega_c = 101$ rpm) for which the agreement between the experiment and the theory is amazing.

In Fig. 10, we show estimates of the amplitude ω_f for $\omega_c = 101$, 207 rpm. Because these determinations rest on accurate measurements of p_c^2, they are spoilt, at small precession rates, by the noise of frequency $2\omega_c$. At larger rates, the results are much more reproducible and we recover the sudden drop in ω_f predicted by the theory.

From the theoretical results (see Fig. 3 and the discussion of the stability of the different branches) we can envision hysteresis. We have looked for such a phenomenon. Because we can tune the rotation rate ω_c much more finely than the precession rate Ω_p, we have kept the latter fixed. Note that high rotation rate then means small precessional forcing. We have chosen a set of parameters (α, Ω_p) such that the range of rotation rates where there are three solutions $\boldsymbol{\omega}_f$ is wide. In Fig. 11, we show results obtained from Doppler anenometry. We start the experiment series with the fastest rotation, decrease ω_c until we observe the abrupt change in the fluid rotation axis and then increase the rotation back to its initial value with the same small increment. We always observe an unique solution for both paths and no evidence of hysteresis. For small ω_c, the velocity measurements are too noisy to yield trustworthy estimates of θ but the transition between two flow regimes occurs at the same rotation rate whether it is approached from small or high

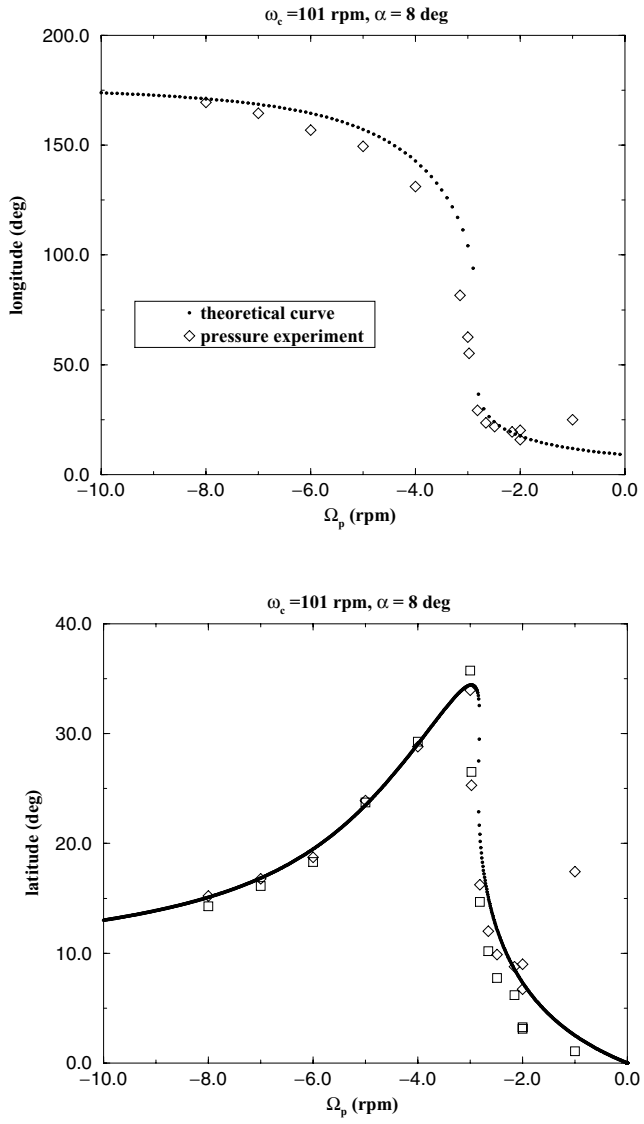

Figure 9. Same as Fig. 7 but for $\alpha = 8^\circ$, $\omega_c = 101$ rpm.

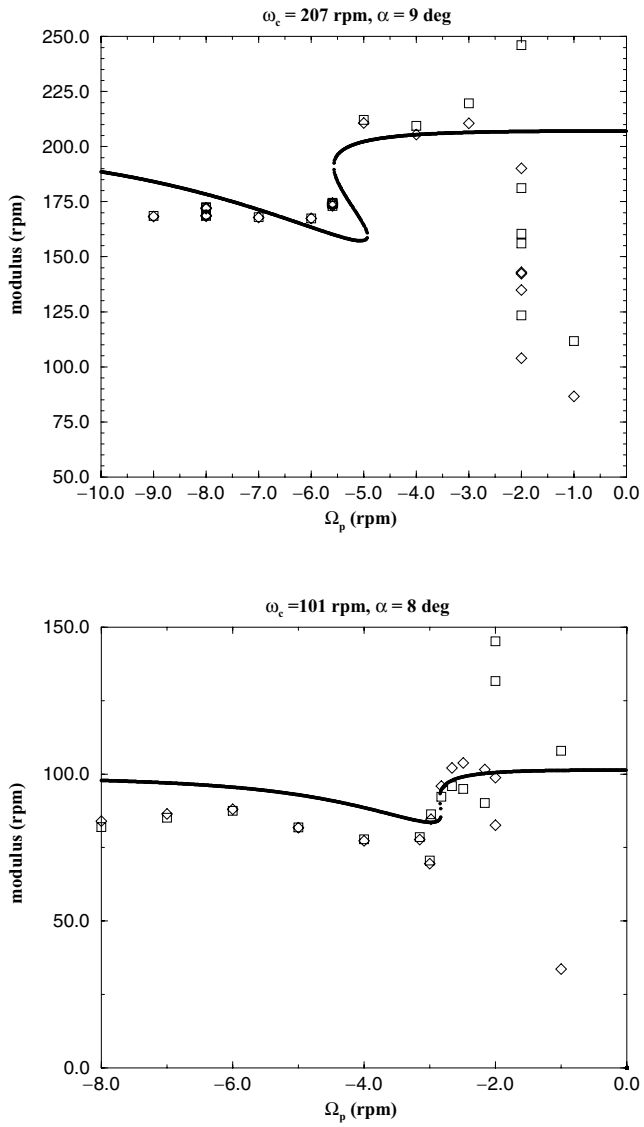

Figure 10. Rotation rate ω_f of the fluid as a solid body. top: $\omega_c = 207$ rpm, $\alpha = 9^\circ$ bottom: $\omega_c = 101$ rpm $\alpha = 8^\circ$.

rotation rates. The change in θ appears very sudden: we have not been able to find intermediate directions.

6 DISCUSSION

Studies of the flow within a slowly precessing cavity yield an experimental illustration of a resonance between the tilt-over eigenmode and a forced oscillation of the cavity axis. When the forcing is strong enough, the linear theory, in which $\omega_f = 1$ is assumed, is not appropriate. As a consequence, it is not possible also to superpose linearly different forcings. Taking into account the finite inclination of the fluid rotation axis with respect to the cavity spin axis in the calculation of the viscous friction, as done by Busse (1968), suffices to yield a qualitative agreement between the theory and the experimental observations.

In an analogous experiment, but with a very large inclination α of the precession axis, Malkus (1968) reported two jumps in the torque on the minor axis of the spheroid for values of 0.5 s^{-1} and 0.78 s^{-1} of precession frequency while we are expecting jumps of $\boldsymbol{\omega}_f$ at 0.2 s^{-1} and 0.75 s^{-1} according to the theory. He showed also that the torque follows an hysteresis loop. In our experiment, we have no evidence of hysteresis. It would be interesting to characterize the conditions that promote such a behaviour since in natural bodies the precessional forcing may reach resonant values either from below or from above as well.

During its history, physical parameters of the Earth's core have changed slowly. Resonances between the tilt-over mode and different nutations (annual, semi-annual,..) should have produced excursions of the axis of rotation of the liquid core (Greff-Lefftz & Legros 1999a). For these resonances, non-linear theory reduces to the linear analysis used by Greff-Lefftz & Legros (1999a,b).

The discovery of the retrograde rotation of the planet Venus has prompted many studies (Goldreich & Peale 1970; Yoder 1995), which take into account resonance between the precession rate and orbital frequencies, atmospheric tides and core-mantle friction. In these works, the core velocity relative to the mantle has been calculated using the linear theory but it is very likely that the conditions for rapid changes of the fluid solid body rotation have been met at

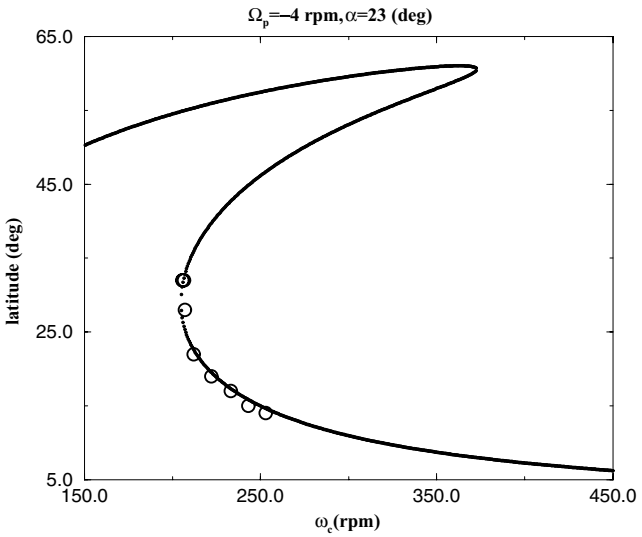

Figure 11. Colatitude θ of the rotation axis of the fluid obtained from Doppler anenometry. $\Omega = -4$ rpm, $\alpha = 23^\circ$.

some stage during the history of Venus. This stimulates us to study how our results can be extended to the small values of the Ekman number that are relevant for the dynamics of the fluid core of planets.

Finally, inclusion of an inner core complicates the description but may be a necessary step to model the rotational dynamics of planetary cores as the non-linear theory illustrated in this paper precludes linear superposition of different effects.

ACKNOWLEDGMENTS

The experiment was funded by programme 'Émergences' of Région Rhône-Alpes. This work was supported also by programme 'Intérieur de la Terre' of CNRS/INSU.

REFERENCES

Busse, F.H., 1968. Steady fluid flow in a precessing spheroidal shell, *J. Fluid Mech.,* **33,** 739–751.

Goldreich, P. & Peale, F., 1970. The obliquity of venus, *Astronomical Journal,* **75,** 273–284.

Greenspan, H.P., 1968. *The theory of rotating fluids,* Cambridge University Press, Cambridge.

Greff-Lefftz, M. & Legros, H., 1999a. Correlation between some major geological events and resonances between the free core nutation and lunisolar tidal waves, *Geophys. J. Int.,* **139,** 131–151.

Greff-Lefftz, M. & Legros, H., 1999b. Core rotational dynamics and geological events, *Science,* **286,** 1707–1709.

Lorenzani, S. & Tilgner, A., 2001. Fluid instabilities in precessing spheroidal cavities, *J. Fluid Mech.,* **447,** 111–128.

Malkus, W.V.R., 1968. Precession of the Earth as the cause of geomagnetism, *Science,* **160,** 259–264.

Manneville, P., 1990. *Dissipatives structures and weak turbulence,* Academic Press, New York.

Noir, J., Jault, D. & Cardin, P., 2001a. Numerical study of the motions within a slowly precessing sphere at low Ekman number, *J. Fluid Mech.,* **437,** 283–299.

Noir, J., Brito, D., Aldridge, K. & Cardin, P., 2001b. Experimental evidence of inertial waves in a precessing spheroidal cavity, *Geophys. Res. Lett.,* **28,** 3785–3788.

Pais, M.A. & Mouël, J.L.L., 2001. Precession-induced flows in liquid-filled containers and in the Earth's core, *Geophys. J. Int.,* **144,** 539–554.

Poincaré, R., 1910. Sur la précession des corps déformables, *Bull. Astr.,* **27,** 321–356.

Stewartson, K. & Roberts, P.H., 1963. On the motion of a liquid in a spheroidal cavity of a precessing rigid body, *J. Fluid Mech.,* **17,** 1–20.

Toomre, A., 1974. On the 'nearly diurnal wobble' of the Earth, *Geophys. J. R. astr. Soc.,* **38,** 335–348.

Vanyo, J.P., Wilde, P., Cardin, P. & Olson, P., 1995. Experiments on precessing flows in the Earth's liquid core, *Geophys. J. Int.,* **121,** 136–142.

Yoder, C.F., 1995. Venus' free obliquity, *Icarus,* **117,** 250–286.